TAF

Journal of Advances in Technology and Engineering Research

JATER

2019, **5**(1): 37-55

PRIMARY RESEARCH

# An advanced electrical approach to gauge rotor position sensors for optimizing electric drive train systems

Christoph Datlinger [1*], Mario Hirz [2]

[1, 2] Institute of Automotive Engineering, Graz University of Technology, Graz, Austria

**Keywords**

Automotive electric powertrain
Resolver rotor position sensor
Transfer function
Impedance
Electrical parameters

**Received:** 7 December 2018
**Accepted:** 10 January 2019
**Published:** 20 February 2019

**Abstract**

This paper introduces a novel, advanced approach to evaluate and benchmark different types of state-of-the-art rotor position sensors for electric drive train systems. It has been well recognized that the reduction of overall emissions produced by transportation systems plays an important role. Cars containing an electrical powertrain are getting more and more widespread in different markets worldwide. Research nowadays is concerned with developing more efficient electrified powertrain systems that can reduce CO2- and harmful emissions. For an efficient and optimized motor control, it is crucial to measure the electric machine's exact rotor angular position and speed. The state-of-the-art rotor position sensor technology used in electric drive trains represents the resolver, which is the investigated sensor type in this research work. To find the most suitable resolver type for a specific powertrain application and so to optimize the overall propulsion control, various kinds of multispeed resolvers from different manufacturers are gauged regarding electrical parameters, that the producer does not define by default. Electrical measurement principles are applied, e.g. to determine the sensor's input and output impedance, establish the transfer function based on the transformer equivalent circuit, specify the phase delay, and the electrical characteristic's temperature behavior. These evaluations are done on a unique, highly accurate sensor test bench and extend the state-of-the-art rotor position sensor characterization [1-4]. The mentioned test bench enables to gauge various kinds of sensors under different mechanical-, speed- and temperature conditions. The new, advanced approach enables a detailed determination of all relevant sensor parameters that are needed to operate an efficient motor control. Furthermore, the methods supports detailed benchmark with the target to determine the most accurate resolver. In addition, the resulting knowledge of the sensor parameters enables further innovative investigations e.g. to determine indirect measured quantities.



## I. INTRODUCTION

Modern society thinking has changed in the past decades to a healthier and more economic lifestyle. This mindset also impels the automobile industry to develop and offer resource-efficient mobility in both individual and public transportation. Research responded to this demand with solutions such as Plug-In Hybrid Electric Vehicles (PHEVs) and Battery Electric Vehicles (BEVs). PHEVs for example achieve fuel savings of 20-50%, when running in urban environment [1, 2, 3, 4]. Due to the fact, that an Internal Combustion Engine (ICE) is operating along the electric drive, a driving range can be reached that is at least equal to a purely fossil driven vehicle. Regarding BEVs, driving range still can be increased when comparing it to PHEVs or conventional cars, which will lead to an increase in sales of BEVs as well. Focusing on individual mobility, the average consumer desires a similar range capability, why research is focused nowadays on the storage of electric energy onboard. Another approach is to increase the overall efficiency of the electric drive train system. For both applications PHEVs and BEVs, precise torque and speed control is crucial to achieve:

- A maximum of driving efficiency, which results in an increased driving range
- Comfort by reducing torque ripple
- Maintaining functional safety-relevant issues

To accomplish a proper synchronization between flux and

*Corresponding author: Christoph Datlinger
†email: christoph.datlinger@tugraz.at

current vector in the electric motor control, an accurate rotor position detection sensor system is required. Besides Hall-based encoder rotor position sensors [5, 6], resolvers are widely used in automotive applications as the state-of-the-art sensor, hence they are robust, durable and accurate [7, 8, 9]. The main focus of this paper is to support the design process of an electric drive train system for both, PHEVs and BEVs by gauging different resolver rotor position sensors in respect to their electrical characteristics (e.g., impedance, parasitic effects, phase- and temperature behavior, etc.). This experimental investigations support a deep understanding in resolver technologies and enable to optimize the Resolver-to-Digital (R2D) interface [10, 11] within the powertrain's Electronic Control Unit (ECU), which helps to select the most suitable resolver for a specific application. This leads to an overall increase of the electric drive control efficiency.

### A. State of the Art Electric Drivetrain

The typical electric drivetrain system including a Permanent Magnet Synchronous Machine (PMSM) consists of four main components (Figure 1): the battery, an ECU including the power electronics, a position sensor and the electric machine. Generally, the system provides a closed-loop based architecture, which means that the ECU controls the electric machine under consideration of the rotary shaft position feedback. The sensor system (e.g., resolver and R2D) is related to the low voltage section of the powertrain. The microcontroller ($\mu$C) within the ECU generates the input signal (see excitation signal in the following subsection) and feeds it into the resolver position sensor. The sensor feedback signals, which contain the angular information, are routed back to the R2D unit of the $\mu$C. Previous studies and optimizations regarding the sensor signal flow chain have been performed in [11, 12, 13]. When designing the sensor's interface of the ECU, it is crucial to have exact knowledge of the resolver's electric behavior. This enables to develop an electronic driver stage that is most suitable for optimal powering the resolver and to design the Analog Front-End (AFE) e.g., filters, for getting the maximum information out of the resolver feedback signals for later angular determination. Hence, the design process shows that it is not always usual to have access to all electric parameters of a resolver, the present paper targets exactly these missing parameters to enable both, a full knowledge of the resolver's characteristic and the capability to optimize the sensor interface (excitation stage and AFE).

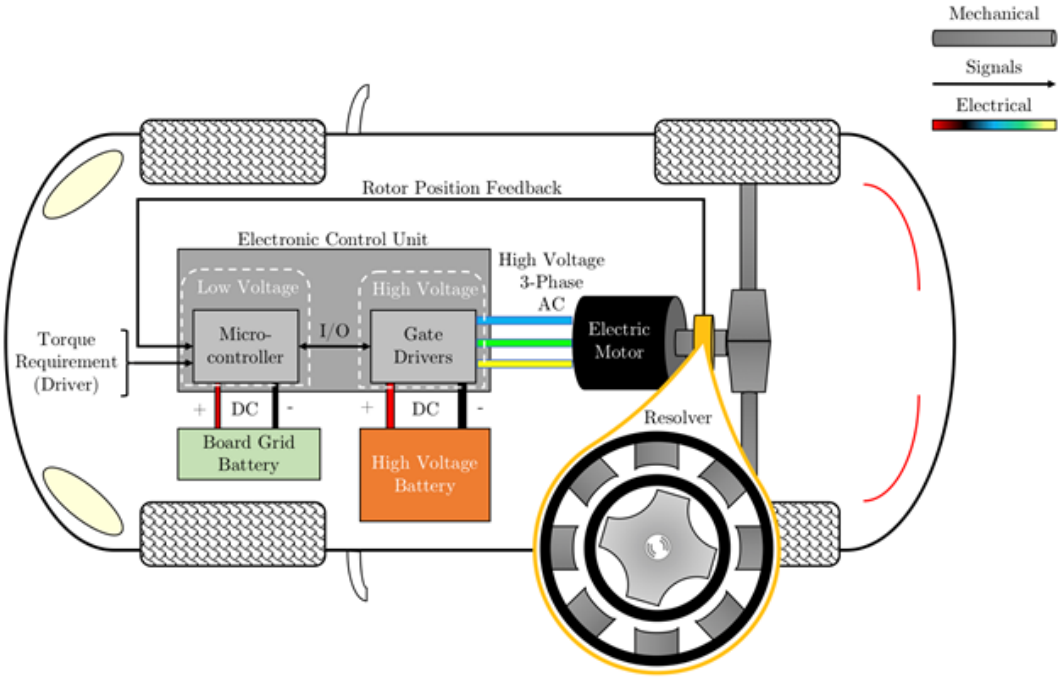


Fig. 1. State of the art BEV drivetrain architecture

### B. Resolver Position Sensor

As stated above, the resolver is commonly used as the state-of-the-art rotor position sensor in electric drivetrains for automotive applications. A Variable Reluctance (VR) resolver consists of three coils, which are described in the following, supported by a graphical representation in Figure 2.

ISSN: 2414-4592
DOI: 10.20474/jater-5.1.4

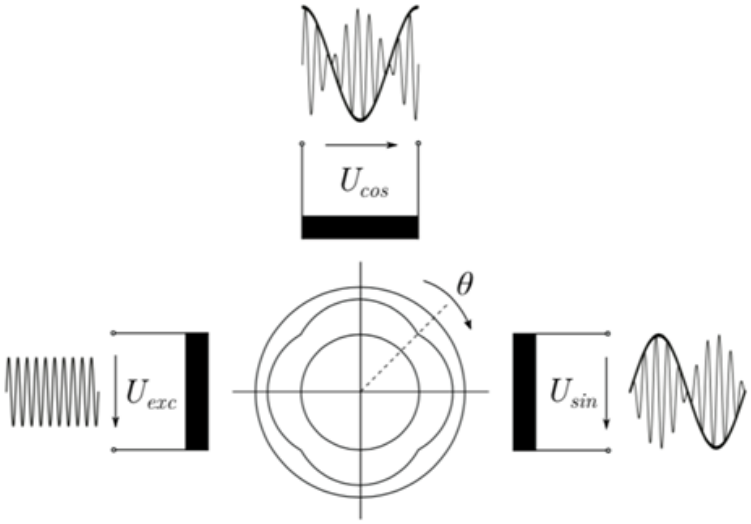


Fig. 2. VR resolver [14]

Because the VR resolver can be stated as a rotating transformer, the primary winding, which is operating as a transmitter, couples an electric field with a high frequency of several Kilohertz (kHz) into the rotor. This field is generated by a sinusoidal excitation signal, that is applied on the primary coil by an electrical voltage $U_{exc}$, stated in (1). The mentioned rotor consists of a stamped, ferromagnetic material. The electric field, which is provided by the primary winding (excitation coil) is coupled through the shape of the rotor. The other two coils are operating as receiver coils, whereby they are mechanically displaced by an angle of 90°. Due to that, one coil is the so-called sine-coil and the other one is the cosine-coil. The receiver coils detect, depending on the position of the rotor, a sinusoidal voltage $U_{sin}$ and $U_{cos}$ as in (2) and (3). As the rotor spins, an amplitude modulated voltage can be measured on both receiver coils (sine- and cosine coil), including the excitation signal (carrier signal) [14, 15, 16].

$$U_{ex} = A \cdot \sin(\omega t) \tag{1}$$

$$U_{\sin} = kA \cdot \sin(\omega t) \cdot \sin(\theta) \tag{2}$$

$$U_{\cos} = kA \cdot \sin(\omega t) \cdot \cos(\theta) \tag{3}$$

For further analysis, the resolver needs to be described electrotechnically in the form of an equivalent circuit. Since the resolver can be considered as a rotary transformer, the equivalent circuit is similar, stated in Figure 3. Fundamental studies in this field have been made, e.g., in [17].

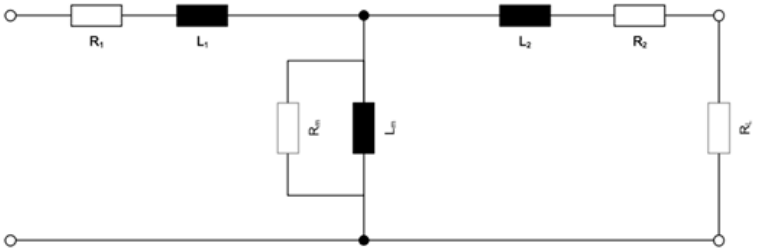


Fig. 3. Equivalent circuit for a VR resolver [17]

Both, the resistor $R_1$ and the inductance $L_1$ describe the primary (excitation) path, whereas the resistor $R_2$ and the inductance $L_2$ represent the secondary circuit (sine- or cosine coil). In between of both sides, a linking inductance is represented by $L_m$, which can be determined by the inductance of both sides. $L_m$ provides the information about the transformation ratio *k*. The resistance $R_m$ depicts the magnetic losses. Under consideration of $Rm >> |L_m|$, the further losses can be neglected. The equivalent circuit is terminated by a termination resistor $R_L$.

## II. DETERMINATION OF THE ELECTRIC SENSOR CHARACTERISTICS

To investigate the resolver's behavior as a black box, the components of the equivalent circuit will be determined in

**ISSN:** 2414-4592
**DOI:** 10.20474/jater-5.1.4

the following. All shown measurements and calculations are performed exemplarily on a resolver with three pole pairs manufactured by [18]. For that reason, this resolver is denoted as "Tamagawa 3x".

### A. DC Analysis

To determine the Ohm's wire resistor of the respective coil (excitation, sine, cosine), the inductance is supplied by a DC-Voltage, shown in Figure 4. The measurand is the current. According to the Ohm's law (4), the Ohm's resistance can be established, exemplified in Table 3.

$$R = \frac{U_{DC}}{I_{DC}} \tag{4}$$

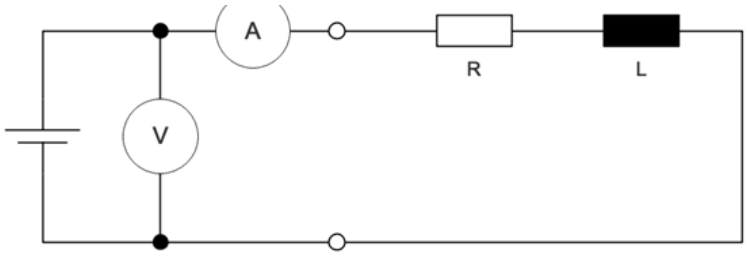


Fig. 4. Schematic of the DC analysis using real coil description (R + L)

TABLE 1
VALUES FOR DC ANALYSIS

| | Set | Measured | Calculated |
|---|---|---|---|
| | $U_{DC}$ [V] | $I_{DC}$C [mA] | R [Ω] |
| Excitation coil | 7 | 734 | 9.54 |
| Sine coil | 7 | 520 | 13.46 |
| Cosine coil | 7 | 470 | 14.89 |

### B. AC Analysis

Applying an AC-voltage and a certain frequency, the total impedance of the respective coil can be determined. Voltage amplitude and frequency are chosen to be equal to the manufacturer's input specifications. Due to the fact, that the inductance is non-ideal, the impedance can be described by (5) as follows.

$$Z_L = R + jX_L \tag{5}$$

Based on the measurement setup shown in Figure 5, the impedance can be established according to (6). The results are illustrated in Table 2.

$$Z_L = \frac{U_{AC}}{I_{AC}} \tag{6}$$

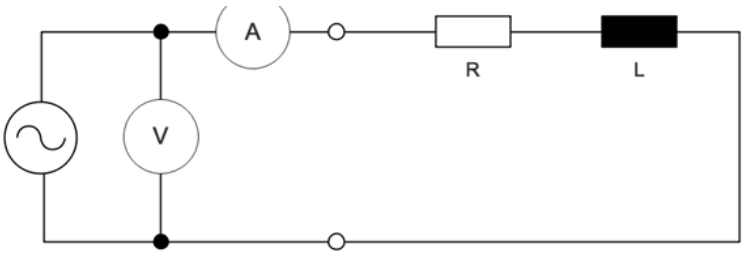


Fig. 5. Schematic of the AC analysis.

TABLE 2
VALUES FOR AC ANALYSIS

| | Set | | Measured | | Calculated |
|---|---|---|---|---|---|
| | U [$V_{pp}$] | f [kHz] | $U_{AC}$ [V] | $I_{AC}$ [mA] | $Z_L$ [Ω] |
| Excitation coil | 20 | 10 | 5.55 | 69.54 | 79.81 |
| Sine coil | 20 | 10 | 6.36 | 46.35 | 137.22 |
| Cosine coil | 20 | 10 | 6.34 | 45.44 | 139.52 |

**ISSN:** 2414-4592
**DOI:** 10.20474/jater-5.1.4

### C. Further Electrical Sensor Parameters

Based on the previous determined parameters *R* and *Z*, the remaining electrical parameters, which describe the sensor electrically can be determined.

The inductive reactance XL deviates from transforming Equation (6).

$$|Z_L|^2 = R^2 + X_L^2 \tag{7}$$

$$X_L^2 = |Z_L|^2 - R^2 \tag{8}$$

$$X_L = \sqrt{|Z_L|^2 - R^2} \tag{9}$$

By substituting *XL* and ω

$$X_L = \omega L \tag{10}$$

$$\omega = 2\pi * f \tag{11}$$

The inductance *L* can be determined as follows:

$$L = \frac{\sqrt{|Z_L|^2 - R^2}}{2\pi * f} \tag{12}$$

Table 3 shows the additional arithmetical determined sensor parameters.

TABLE 3
FURTHER DETERMINED ELECTRIC PARAMETERS

| | Measured | | | | Measured | | |
|---|---|---|---|---|---|---|---|
| | $U_{AC}$ [V] | $I_{AC}$ [mA] | $U_{DC}$ [V] | $I_{DC}$ [mA] | $Z_L$ [Ω] | R [Ω] | L [Ω] |
| Excitation coil | 5.55 | 69.54 | 7 | 734 | 79.81 | 9.54 | 1.26 |
| Sine coil | 6.36 | 46.35 | 7 | 520 | 137.22 | 13.46 | 2.17 |
| Cosine coil | 6.34 | 45.44 | 7 | 470 | 139.52 | 14.89 | 2.21 |

Another essential parameter is the coupling inductivity $L_m$. By applying the transformation ratio *k* and both inductivities $L_1$ and $L_2$, the coupling inductivity can be determined as follows, whereby $L_1$ represents the excitation windings and $L_2$ represents either sine or cosine windings.

$$L_m = k * \sqrt{L_1 * L_2} \tag{13}$$

The transformation ratio can be determined by the manufacturer specifications or by measuring the voltage ratio between input- and output voltage (e.g., excitation to cosine).

### D. Transfer Behavior (Bode)

By applying the Two-port-Network Theory [19, 20], the transfer behavior of the sensor can be established. By usage of the equivalent circuit (Figure 3), the polynomial form arises to (13).

Figure 6 graphically represents the result of the transfer function using a bode plot.

$$G(S) = \frac{s * L_m * R_L}{s^2 \left(L_1 L_2 R_1 + L_1 L_m R_1 + L_2 L_m R_1\right) + s \left(L_1 R_2 + L_m R_2 + L_2 R_L + L_m R_L + L_1 + L_m\right) + R_1 R_2 + R_1 R_L} \tag{14}$$

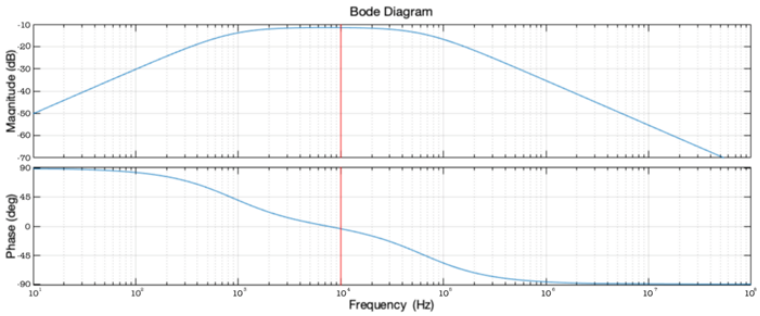


Fig. 6. Transfer function of the 3x Resolver for cosine path at $\theta$ = 0°.

ISSN: 2414-4592
DOI: 10.20474/jater-5.1.4

Upper Figure 6 shows the transfer function of the cosine output path at a mechanical and electrical position of $\theta$ = 0°. The red cursor in the bode plot represents the operating frequency of $f_{exc}$ = *10kHz*. The diagram shows that the resolver sensor acts as a first order bandpass filter. The cut-off frequencies are $f_{c,1}$ = *8 45Hz* and $f_{c,2}$ = *65.4kHz*. Because the frequency fexc is within these frequencies, it is proven that the resolver operates in a stable range and the phase displacement is ≈ 0°. To validate the mathematical model, the resolver was electrically simulated in PSpice [21] with the measured parameters. Figure 7 represents the simulated equivalent circuit for the cosine output, while Figure 8 illustrates the amplitude- and phase response. The fundamental parameters for the simulation stem from the previous analysis (see Table 3).

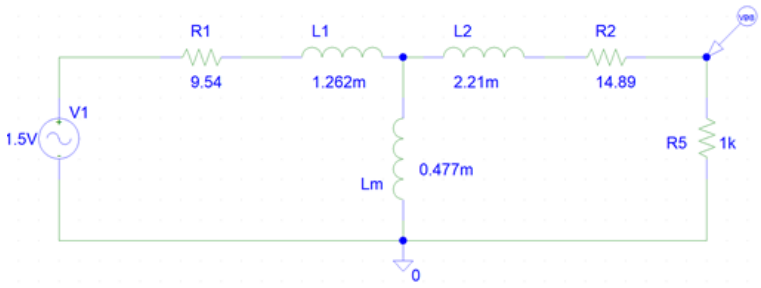


Fig. 7. Simulated sensor based on the equivalent circuit for the cosine path

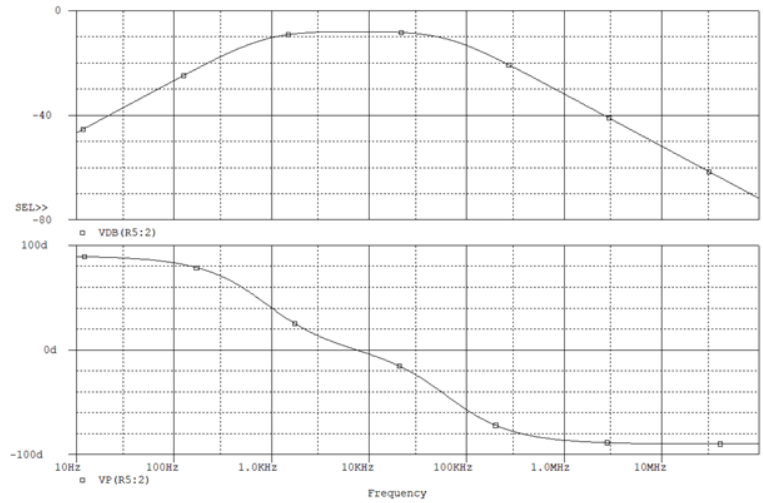


Fig. 8. Bode plot of the resolver's electrical simulation in PSpice

When comparing the results of the mathematical model in Figure 6 with the electrical simulation in Figure 8, it can be seen that apart from slight deviations both, the mathematical representation and the electric model, based on performed measurements, correspond to each other. To verify the resolver's electrical phase, a sinusoidal voltage is applied on the excitation input. The phase shift between the sinusoidal input and output voltage is measured with an oscilloscope. By varying the input frequency fexc a phase shift of $\phi = 0°$ can be found. For the exemplary resolver, this point occurs at $f_{exc}$ = *9.765kHz*, which deviates slightly from the manufacturer's specifications of $f_{exc}$ = *10kHz* as also stated in the bode diagrams. In this way, the ideal operating point of this resolver can be easily determined by these methods and set in an ECU.

### *E. Parasitic Effects*

One way to explain the slight discrepancy between measurements and simulation results includes the parasitic effects that appear in each electronic component. For most of the electrical dimensioning cases, these effects are neglected, hence the influence is low. For a detailed analysis it is crucial to consider the parasitic effects of the rotor position sensor in an electric drive train. That enables to develop an optimal setup for a specific powertrain application. In the following subsequence, the parasitic effects of the exemplary resolver are studied.

**ISSN:** 2414-4592
**DOI:** 10.20474/jater-5.1.4

When considering a real inductance, a further component beside of the Ohm's proportion appears in form of a parasitic capacity. This is because each electrical conductor also contains a small capacity part. The parasitic capacity can be represented in the equivalent circuit in a parallel connection to the wire resistance *R* and the inductive reactance *L*. The capacity of interest can be determined by making use of the parallel resonant circuit's characteristic. Every resonant circuit has, depending on the order, at least one resonant frequency $f_0$. By applying a frequency sweep, the resonant frequency $f_0$ can be identified, which enables to determine the desired capacity based on calculations performed in the subsequence Further electrical sensor parameters. Figure 9 illustrates the measurement setup.

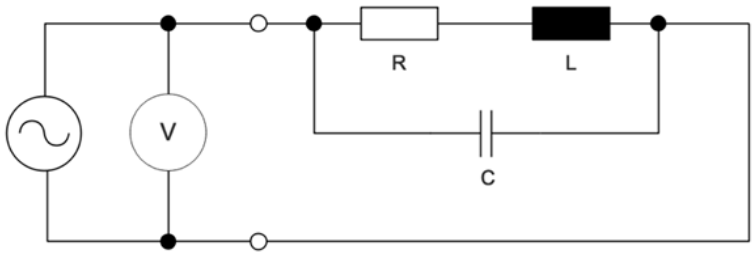


Fig. 9. Measurement setup to identify the parasitic capacity

For each output path (sine and cosine), the capacity was determined separately. As stated, the frequency of the sinusoidal voltage is varied until the measured voltage reaches a maximum. This is where the resonance occurs at $f_0$. The equations (14) to (5) outline the establishment of the parasitic capacity, while Table 4 shows the determined capacity values for each coil.

TABLE 4
PARASITIC CAPACITY VALUES DETERMINED

| | Set | Measured | Calculated | |
|---|---|---|---|---|
| | $V_{pp}$ [V] | $V_{RMS}$ [V] | $f_0$ [kHz] | C [pF] |
| Excitation coil | 20 | 6.953 | 457 | 96.11 |
| Sine coil | 20 | 6.904 | 77 | 2000 |
| Cosine coil | 20 | 6.918 | 73 | 2000 |

$$f_0 = \frac{1}{2\pi * \sqrt{LC}} \tag{15}$$

$$C = \frac{1}{4\pi^2 * f_0^2 * L} \tag{16}$$

By transferring the parasitic effects into the resolver's equivalent circuit (Figure 10), the transfer function can be described as stated in (16). This description leads to the bode plot in Figure 11 (orange line).

$$\begin{aligned} G(s) = {} & (s * L_m * R_L) \,/\, \left(s^4 \left(C_1 C_2 L_2 L_m R_1 R_2 + C_1 C_2 L_2 L_m R_R R_L\right)\right. \\ & + s^3 \left(C_2 L_2 L_m R_2 + C_2 L_2 L_m R_L + C_1 C_2 L_1 L_2 R_1 R_2 + C_1 C_2 L_1 L_2 R_1 R_L\right) \\ & + s^2 \left(C_1 L_m R_1 R_2 + C_1 R_1 R_L L_m + C_2 L_2 R_1 R_2 + L_2 C_2 R_1 R_2 + C_2 R_1 R_2 L_m\right. \\ & + s \left(R_2 L_m + R_L L_m + C_2 L_m R_1 R_2 + L_1 C_1 R_1 R_2 + L_1 C_1 R_1 R_L + L_2 + 2 L_m\right) \\ & \left. + R_1 R_2 + R_1 R_L\right) \end{aligned} \tag{17}$$

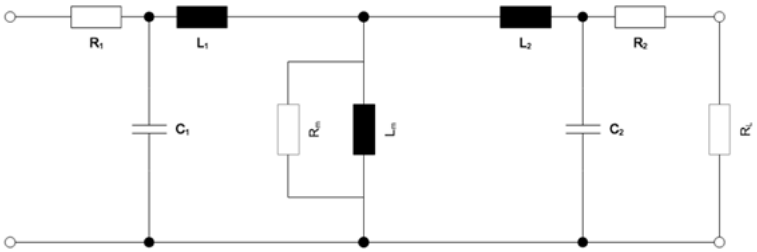


Fig. 10. Complete equivalent circuit of the resolver including parasitic effects on primary and secondary windings

ISSN: 2414-4592
DOI: 10.20474/jater-5.1.4

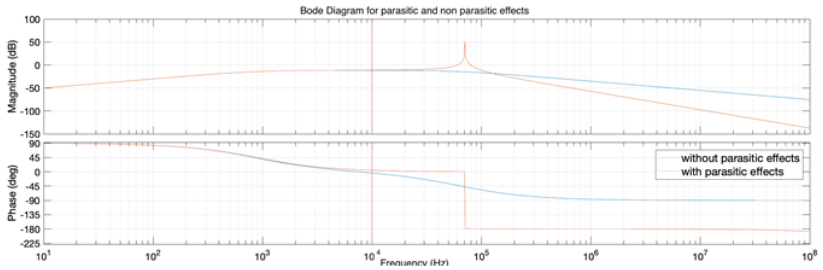


Fig. 11. Comparison of parasitic and non-parasitic effects in the transfer function, represented graphically in a bode plot

The resonance at $f_0$ = *70kHz* can be clearly seen in Figure 11 (peak of the orange line). It can also be seen, that the behavior of the sensor's band pass filter characteristic changes from first order to fourth order, due to a higher damping characteristic $(D \approx 40dB/decade)$ in the low pass area. Further, the phase turns to $\phi = -180°$. When considering the operating point of the resolver (red horizontal marker in Figure 11), the parasitic effects do not have a big influence on the resolver's behavior.

The introduced method enables to evaluate the parasitic effects of the resolver and to decide, whether these effects have an influence on the sensor's performance or not. With this information, the excitation frequency can be adjusted to optimize the sensor system.

### *F. Amplitude Response*

Hence the rotary part of the resolver is in motion while operating the drive train system, this section introduces a method to investigate the amplitude response under consideration of rotation. The main difference between this method and the previous investigations is, that now the cosine is not at a maximum anymore ($\theta \neq 0^o$). For this analysis, the bode plot is again the tool of interest. By varying the absolute rotary position, the transformation ratio $k$ (17) can be determined, which enables to evaluate the transfer function for any rotary position, since the transformation ratio k is an essential component of the coupling inductivity, see (12).

$$k = \frac{U_{\text{out}}}{U_{\text{in}}} = \frac{U_{\text{sin}}}{U_{\text{exc}}} = \frac{U_{\text{cos}}}{U_{\text{exc}}} \tag{18}$$

Note that all investigated resolvers, including the exemplary type, are multipole resolvers. For that reason, only one electrical revolution, which depends on the number of pole pairs, is investigated in this work. If the resolver has a pole pair amount of e.g., three, the electrical revolution repeats every $\theta_{mech} = 120^o$. So, in three electrical revolutions, one mechanical revolution is completed. As illustrated in Figure 12, the bandpass filter characteristic is unchanged over an electrical revolution. However, an amplitude damping occurs depending on the rotary position, while the phase behaves as expected from slight deviations over the full frequency range. The higher damping of $D = -40dB$ (see Figure 12: light blue and light green) appears at those rotary positions, where the cosine coil absorbs the minimal excitation voltage Uexc. Considering an ideal resolver, the damping factor *D* is assumed as infinite.

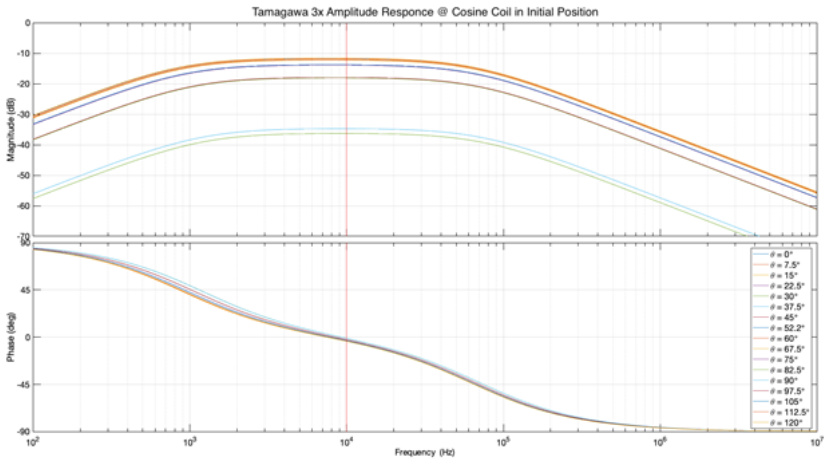


Fig. 12. Exemplary bode plot of the amplitude- and phase response for the cosine resolver output under different electric angular positions

**ISSN:** 2414-4592
**DOI:** 10.20474/jater-5.1.4

The previous investigation assumed an ideal mechanical adjustment of the resolver's rotor and stator. In succession, the rotor is displaced in respect to the stator on a dedicated rotor position test bench [11, 12, 13, 14] at the Institute of Automotive Engineering Graz [22]. The investigations of the amplitude response under misaligned conditions are performed within a range of $x = y = \pm 0.25mm$. Hence the receiver coils sine and cosine are displaced in relation to the theoretical center point (sweet spot), the magnetic flux within the resolver is changing when passing from the excitation coil through the shape of the rotor. For that reason, the transformation ratio changes significantly compared to the initial position (see Figur 13).

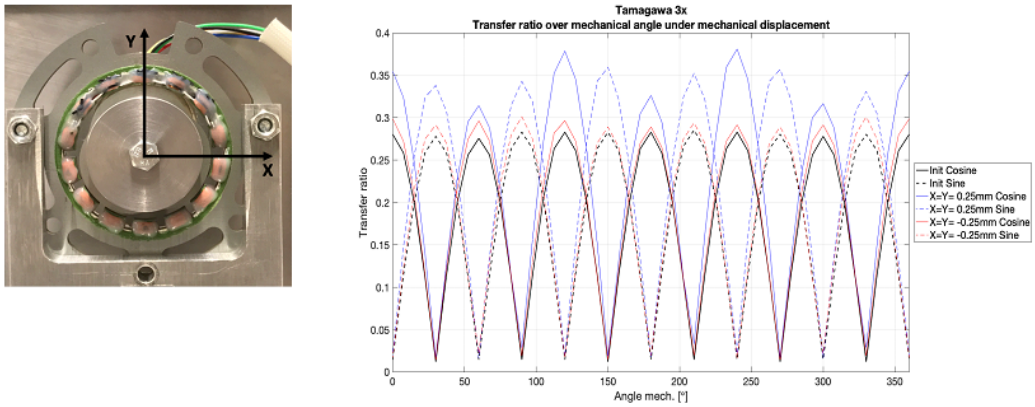


Fig. 13. Exemplary investigated three pole resolver with coordinate system for misalignment (le.); transfer ratio over mechanical angle in initial- and misaligned position (ri.)

For the sake of completeness, Figure 14 illustrates the amplitude- and phase response for a positive offset $x = y = +0.25mm$ based on the transformation ratio measurements. It has to be noted, that there is no big difference compared to the initial position (Figure 12), hence these changes do not affect the bandpass filter behavior in a major way.

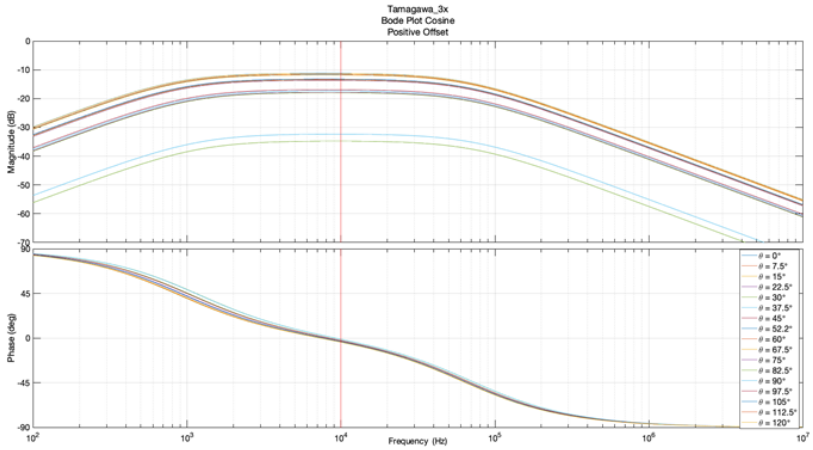


Fig. 14. Bode plot of the resolver's transfer function on cosine output coil with a positive mechanical offset of $x = y = +0.25mm$

### G. *Phase Analysis*

The former analysis followed up with investigating the amplitude response under certain conditions. Because slight phase deviations can occur (see Figure 12 and Figure 14), it is crucial to examine the resolver's phase behavior in both, static and operational conditions. The phase analysis results can be used for further investigations, e.g., to analyze and compensate delays and runtime errors in the complete measurement chain of the sensor system. The following section introduces three experimental methods regarding phase relation analysis in operational mode based on previous research in this field [23, 24]. State-of-the-art measurement equipment e.g., oscilloscopes with integrated phase measurement algorithms are unsuitable, since the cost fac-

**ISSN:** 2414-4592
**DOI:** 10.20474/jater-5.1.4

tor plays an important role and the applied online algorithms are not compatible with amplitude modulated signals unless it is possible to extract the envelope signal out of the sensor signal. The latter can only be achieved if exact knowledge about the carrier signal is guaranteed. When the rotary part of the resolver is rotating with the angular speed of the electric machine's shaft, the analog sensor feedback signals deliver an amplitude modulated AC signal with a carrier frequency equal the excitation frequency e.g., $f_{exc}$ = *10kHz*. The overall frequency of the amplitude modulated signal is corresponding with the electrical rotational speed of the resolver and can be converted easily to the mechanical speed in consideration of the sensor's pole pairs. Since the overall frequency (e.g., electrical rotational frequency) can be a multiple higher than $f_{exc}$, fast electronics switching times are required [11, 12].

*1) Phase determination using XOR-gate:* With this method, two phase shifted sinusoidal signals are converted in square wave signals by the use of a comparator. The comparator outputs are fed into an XOR-gate, which generates an Puls Width Modulated (PWM) signal. In case of a higher duty cycle *D*, the phase shift between the input signals increases. Is the duty cycle lower, the phase shift is lower. A duty cycle of *D=0%* means no phase shift at all (both signals are synchronous). To validate the PWM signal, a Low Pass Filter (LPF) is used, providing a smoothed output voltage. This output voltage is proportional to the phase shift of the input signals. Figure 15 exemplifies the block diagram and the signals. Both, the reference signal (e.g., carrier signal) and the measurement signal (e.g., resolver cosine output) are fed into one comperator per signal path. In the present exemplary application, a fast Operational Amplifier (OPAMP) with an open collector output is used as the mentionted comperator type [25]. The applied XOR-gate has the property of fast reaction times [26]. The filter at the output of the XOR-gate contains a multiple set of first-order LPFs to achieve an appropriate high damping.

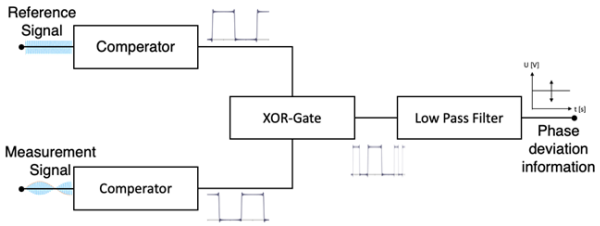


Fig. 15. Block diagram of the phase measurement setup using a XOR-gate

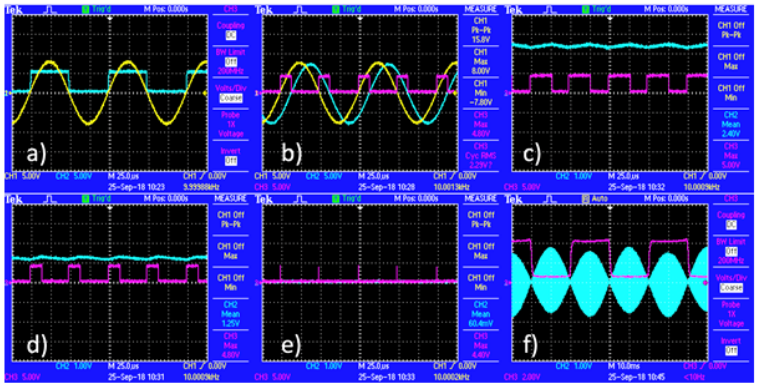


Fig. 16. Results of phase analysis using XOR-gate: a) Sinusoidal input signal (yellow); Comparator output (cyan) – triggering the positive half period of the sine wave. b) Output of the XOR-gate (magenta) – shows phase shift of the reference- and measurement input signals (yellow and cyan). c) to e) Output of the XOR-gate (magenta) and filtered phase deviation signal (cyan) – the voltage level changes in respect to the phase shift. f) Phase shift measurement while resolver rotation: voltage jumps to $U_{phase} \approx 2V$ are caused by a phase turn of $\varphi = 180^{o}$ in the amplitude modulated sensor feedback signal (high time must be ignored in this case).

Now that a phase shift depending voltage is generated by the developed circuit, this voltage needs to be allocated with a certain, occurring phase shift. For that reason, the circuit is fed with a sinusoidal signal (measurement signal) performing a phase delay sweep to generate a look-up table for later measurements. According to (18), based on the signal time delay $\Delta T$, the phase delay (also called phase lag) can be determined. Table 5 represents the resulting phase shift

**ISSN:** 2414-4592
**DOI:** 10.20474/jater-5.1.4

look-up table representing the input delay with respect to the reference signal in [ns], the resulting phase lag in [°] and the corresponding circuit's output voltage in [mV].

$$\varphi = 360° * f * \Delta T \tag{19}$$

TABLE 5
PHASE SHIFT LOOK-UP TABLE

| Phase-Shifted Input | | Output Voltage[mV] |
|---|---|---|
| ΔT [ns] | Phase lag [°] | |
| 350 | 1.26 | 83 |
| 500 | 1.8 | 98 |
| 750 | 2.7 | 128 |
| 1000 | 3.6 | 158 |
| 2000 | 7.2 | 281 |
| 3000 | 10.8 | 389 |
| 4000 | 14.4 | 499 |
| 5000 | 18 | 588 |
| 7500 | 27 | 824 |
| 10000 | 36 | 1081 |

Subsequently, the determined output voltage, which is according to the phase shift, can be graphically illustrated by a reference curve, shown in Figure 17. It can be seen, that the phase depending voltage and so the circuit, have a linear behavior. Both, the look-up table (see Table 5) and the reference curve (see Figure 17) can be used to determine the phase delay of an arbitrary measured input signal.

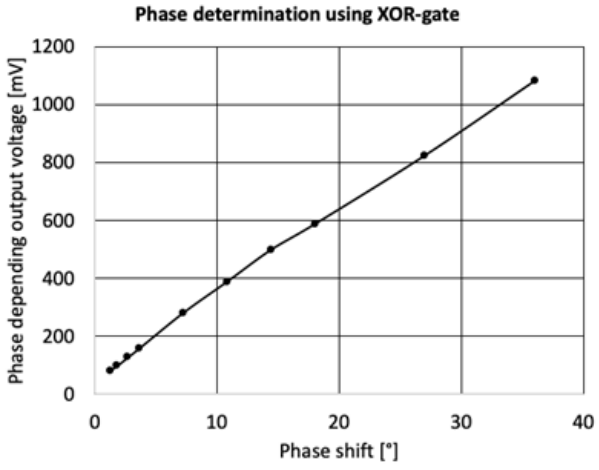


Fig. 17. Phase depending output voltage of the XOR-gate-based phase measurement method

For static, non-rotational analysis, the introduced method enables a precise phase lag determination. It seems, that this approach is suitable for gauging the resolvers output signal phase deviation with respect to the input signal. As stated in Figure 16, the phase information voltage toggles while the resolver is operating in rotation. This is caused by the amplitude modulated resolver feedback signal. Certainly, it can be taken into account to only validate one half-period of the measurement signal. For that reason, a second mathematical approach is investigated and described in the following.

*2) Phase determination using multiplication of two signals:* Two sinusoidal signals can be multiplied as stated in (19). Considering the time course of both, the reference signal $S_{ref}(t)$ (20) including the phase shift $\Delta\varphi$ and the measurement signal $s_{mes}(t)$ (21), the multiplication results in *p(t)* (22).

$$\sin(\alpha) * \sin(\beta) = \frac{1}{2}[\cos(\alpha - \beta) - \cos(\alpha + \beta)] \tag{20}$$

$$s_{ref}(t) = A_{ref} + \sin(\omega t) \tag{21}$$

$$s_{mes}(t) = A_{mes} * \sin(\omega t - \Delta\varphi) \tag{22}$$

$$p(t) = \frac{A_{ref} * A_{mes}}{2}[\cos(\omega t - \omega t + \Delta\varphi) - \cos(\omega t + \omega t - \Delta\varphi)] \tag{23}$$
$$= \frac{A_{ref} * A_{mes}}{2}[\cos(\Delta\varphi) - \cos(2 * \omega t - \Delta\varphi)]$$

Therefore, the resulting output signal *p(t)* consists of an oscillation having the doubled frequency, including a direct component in form of a cosine function. This cosine function contains the phasing information. To remove the irrelevant oscillations, a LPF can be used. In case both signals are in phase, the output signal *p(t)* (also Uphase) reaches its peak value. However, to provide $U_{phase} = 0V$ in this scenario, one signal is shifted by $\varphi$ = 90°, see (23) and (24) [23].

$$p(t) = \sin(\alpha) * \sin(\beta + 90°) = \sin(\alpha) * \cos(\beta) \tag{24}$$
$$= \frac{1}{2}[\sin(\alpha - \beta) - \sin(\alpha + \beta)]$$

$$p(t) = \frac{A_{ref} * A_{mes}}{2}[\sin(\Delta\varphi) - \sin(2 * \omega t - \Delta\varphi)] \tag{25}$$

By using the previously established look-up table (Table 5) and reference curve (Figure 17), the phase shift can be interpreted. The main difference and advantage compared to the previous method (see Figure 15) is the great linearity in the range of $\varphi$ = 0°. Slight deviations can so be detected at once.

For practical realization, illustrated in Figure 18, a hardware based all-pass filter is used as phase shifter at the reference signal. The multiplication of both sinusoidal signals is achieved by a hardware analog multiplier [27]. As before,

**ISSN:** 2414-4592
**DOI:** 10.20474/jater-5.1.4

the output of the multiplier is filtered by a LPF. Figure 19 shows exemplary the results for both in-phase signals and phase shifted signals.

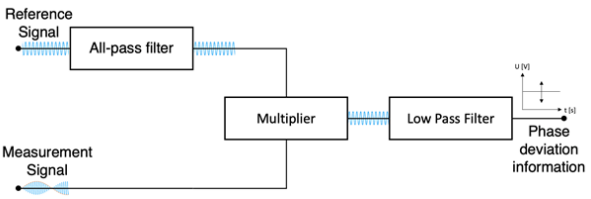


Fig. 18. Block diagram of the phase measurement setup using a multiplier

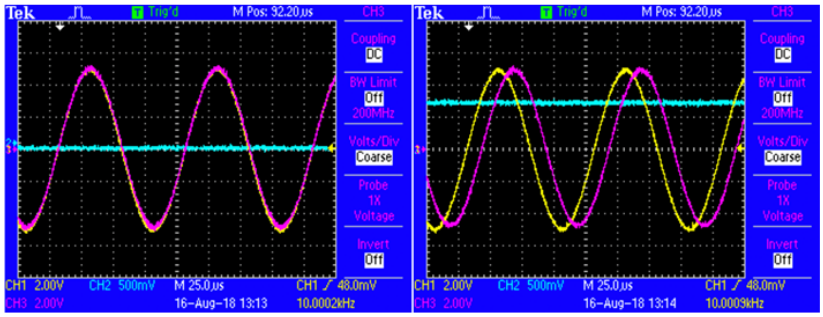

Fig. 19. Phase depending output voltage (cyan) of multiplier circuit, measurement signal (magenta), reference signal (yellow): $U_{phase} = 0V$ when $\Delta\varphi = 0^{o}$ (le.); $U_{phase} \approx 700mV$ when $\Delta\varphi \approx 20^{o}$ (ri.)

Note that in case of rotation an additional factor *cos(θ)* is added to the output voltage $U_{phase}$ when multiplying an amplitude modulated resolver feedback signal by a reference signal with $f_{ref}$ = *constant* and $A_{ref} = constant$, see (25) and (26). By extracting the electrical rotational frequency of the resolver *θ*, the phase shift can be determined. Hence, this can require much computational power, a third approach is investigated, introduced in the following section.

$$p(\mathrm{t}) = \cos(\theta) * \sin(\alpha) * \sin(\beta + 90^{\circ}) \qquad (26)$$
$$= \cos(\theta) * \sin(\alpha) * \cos(\beta)$$
$$= \cos(\theta) * \frac{1}{2}[\sin(\alpha - \beta) - \sin(\alpha + \beta)]$$

$$p(t) = \frac{A_{ref} * A_{mes}}{2}[\sin(\Delta\varphi) - \sin(2 * \omega t - \Delta\varphi)] \qquad (27)$$

*3) Phase determination by approximation:* Another option to determine the phase deviation for both, static and rotational operation is to measure the resolver's input- and output signal's transit time difference. By making use of (18), a phase shift $\Delta\varphi$ can be determined. In addition, the bode plot of the measured transfer function (e.g., Figure 12 or Figure 14) supports the phase shift analysis at rotational operation. Figure 20 exemplary illustrates a rotational phase shift measurement based on this method. The data derives from both, transit time difference measurements and the bode plot. For further investigations, the mean value of the phase shift is determined (see black line, Figure 20). For the purpose of validation, the sensor's phase deviation limits around the mean value, obtained by the datasheet, are figured (see red dashed border lines, Figure 20).

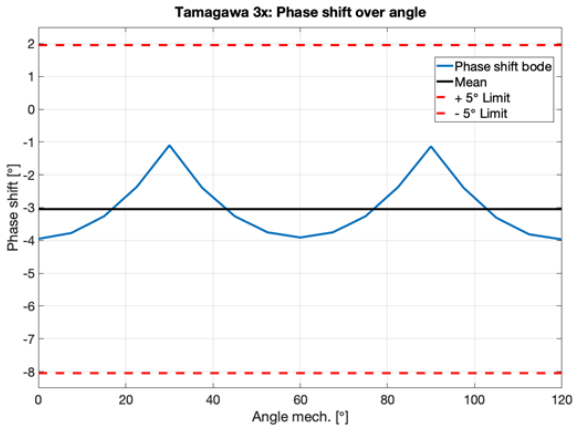


Fig. 20. Phase shift evaluation for rotational operation using transit time- and transfer function measurements

### H. Temperature Behavior Analysis

Hence the resolver is integrated in the drive train, the sensor has to withstand a wide temperature range besides of shock and vibrations (see misalignment analysis, Figure 13). For that reason, electrical sensor parameter investigations are made under influence of different ambient temperature. The previous introduced electrical characterization methods are applied for these evaluations. In this way, measurements are applied on the mentioned rotor position sensor

**ISSN:** 2414-4592
**DOI:** 10.20474/jater-5.1.4

test bench. Thereby, the resolver is mounted on the rotary shaft of an electric test bench drive, surrounded by a temperature chamber providing an ambient temperature range of $T = -40^oC$to $T = +60^oC$. Figure 21 gives an overview of the overall test bench setup used in this work.
The first gauging includes static investigations of the resolver's transfer ratio over one electrical revolution under influence of temperature, illustrated in Figure 22.

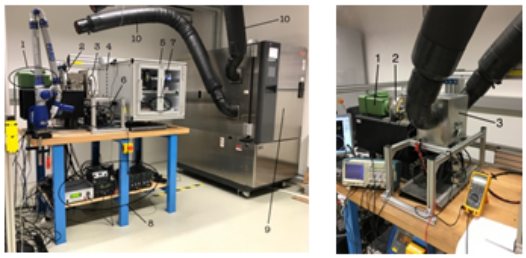

(a) (b)

Fig. 21. Test bench setup: (a) 1: Electric drive; 2: Reference sensor; 3: Resolver; 4: Temperature chamber (removed for demonstration-see dashed box); 5: Data acquisition housing (incl. EMC shielding); 6: Motorized positioning actuators; 7: Resolver excitation stage; 8: Controlled power supply; 9: Climatic chamber (temperature conditioning); 10: Thermal tubes (for thermal transfer); (b) 1: Electric drive; 2: Reference sensor; 3: Temperature chamber surrounding the resolver

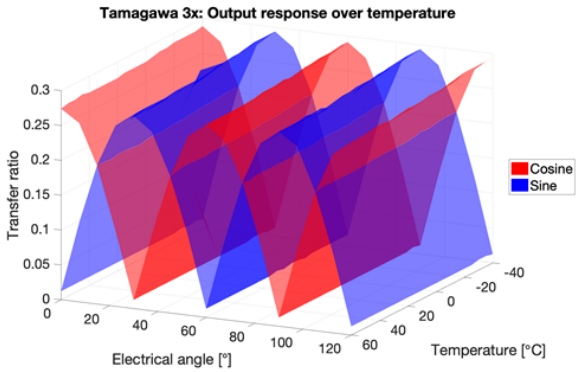


Fig. 22. Temperature depending transfer ratio under consideration of rotary variation.

The result (Figure 22) shows, that the output characteristic of the investigated resolver type stays constant over a tested temperature difference of $\Delta T = 100^oC$. So, the measurements approve that the resolver has a great robustness regarding temperature changes. Since the drive train system also comprises miscellaneous temperature sensors that monitor temperatures such as bearings-, electric drive- or rotor shaft temperatures, the following investigations consider the indirect measurement of the rotor shaft temperature using the resolver. This method provides redundant function (e.g., for functional safety-related issues) or the possibility to reduce the amount of temperature sensors in the drive train system. By use of the former introduced DC analysis, the Ohm's resistance of the resolver output coils sine and cosine are investigated under temperature change. Hence, the resistance value is temperature depending, the electrical current also changes, according to Ohm's law (4). An increase of the temperature causes an increase of the coil's resistance and so the electrical current decreases. Figure 23 illustrates the DC measurements of the resolver's temperature depending resistance. Though the resistance change is in a small range, a linear characteristic can be seen.

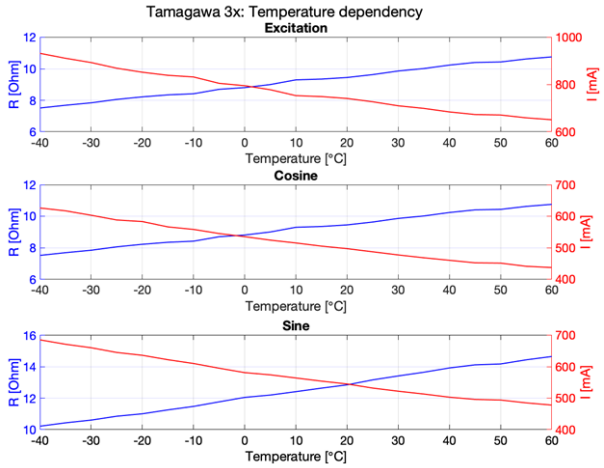


Fig. 23. Resistance dependency temperature investigation for excitation-cosine- and sine coil

In terms of linear regression, a line of best fit can be determined for the measurement values. This leads to a linear function (27). The coefficients can be determined according to (28) and (29).

$$y = kx + d \tag{28}$$

$$k = \frac{\sum_{i=1}^{n} (x_i - \bar{x})(y_i - \bar{y})}{\sum_{i=1}^{n} (x_i - \bar{x})^2} \tag{29}$$

$$d = \bar{y} - k * \bar{x} \tag{30}$$

Whereby *n* represents the numbers of measurements and its mean values are written as $\bar{x}$ and $\bar{y}$. The accuracy of the results can be increased by a high frequency of measurements repetition. Figure 24 shows the results of the linear regression on each resolver coil.

**ISSN:** 2414-4592
**DOI:** 10.20474/jater-5.1.4

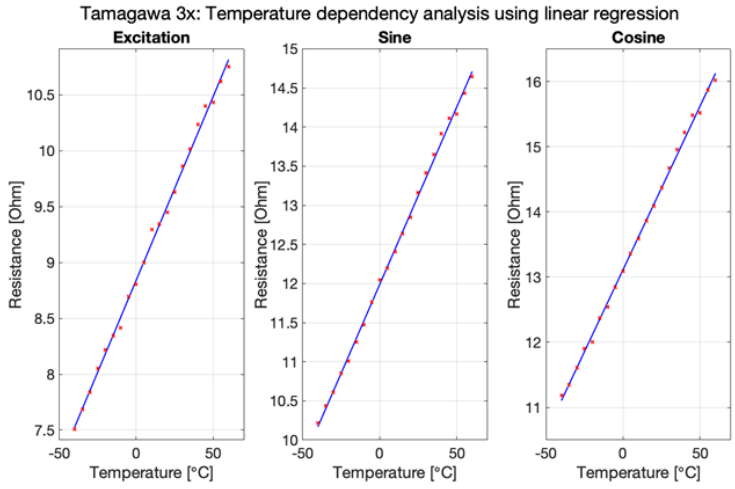


Fig. 24. Applied linear regression analysis for temperature-depending resistance measurements on the resolver

Now that it has been proven by performed measurements that a temperature change can be detected by observing the resolver's electrical resistance, a further investigation addresses the change of the resolver's transfer function under different temperature conditions. Therefore in a first run, temperature sweep measurements are performed to determine the output coils resistance and inductance. Subsequently, these values are used to accomplish a simulation of the resolver's temperature depending transfer function, which can be visualized using the bode plot in Figure 25. The results show, that the applied temperature only affects the lower cut-off frequency $f_{c,1}$.

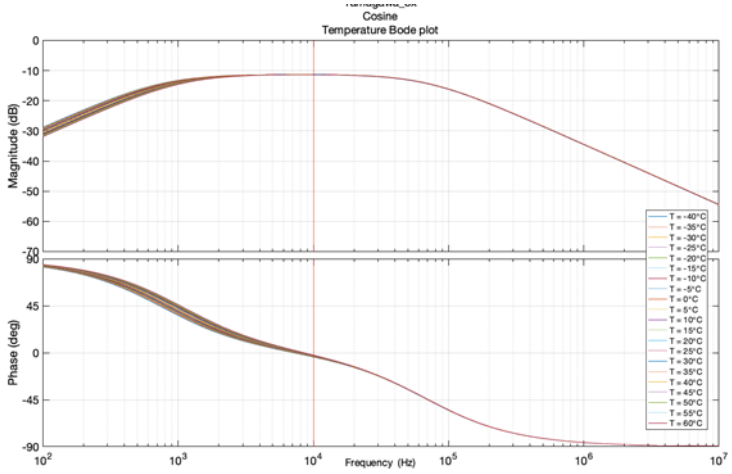


Fig. 25. Bode plot of the temperature depending transfer function

This leads to the statement, that temperature can be measured indirectly over the coil-resistance, however, the overall sensor characteristic stays unchanged according to temperature (great sensor robustness).

## III. BENCHMARK OF VARIOUS SENSOR SAMPLES

The previous introduced analysis method provides a detailed determination of various sensor parameters. As a result, these investigations are applied to a multiple set of resolver position sensor samples with a different number of pole pairs and different mechanical sizes (diameter). Figure 26 gives an overview of the examined sensors and their determined parameters, whereas the Sensor Sample 1 represents the exemplary examined resolver (Tamagawa 3x). The electrical parameters include transformation ratio, input impedance and for some sensor samples the output impedance and the phase shift. Other important parameters are undefined by the manufacturer and need To Be Defined (T.B.D.) on test bench. The determined parameters according to the introduced methods are in range of the sensor's specifications, when comparing the given param-

**ISSN:** 2414-4592
**DOI:** 10.20474/jater-5.1.4

eters with the determined parameters (see green cells, Figure 26). This proves that the performed analyses are comprehensible and applicable for every resolver.

To illustrate the different electric parameters of each resolver sample, the investigation results are combined in Figure 26 to Figure 28.

| | | | Sensor Sample #1 | | | Sensor Sample #2 | | |
|---|---|---|---|---|---|---|---|---|
| | | | Datasheet | | Validation | Datasheet | | Validation |
| Poles | | | 3 | | | 3 | | |
| Input Voltage | | | AC 7 Vrms 10 kHz | | | AC 7 Vrms 10 kHz | | |
| Transformation Ratio | | | 0.286 ± 10% | | 0.2805 | 0.286 ± 10% | Target ±5% | 0.28 |
| Input Impedance | Z | | 75 Ohm ± 10% | | 79.81 | 110 Ohm ± 10% | | 99.15 |
| | L | | ----- | | 1.26 | ----- | | 1.558 |
| Output Impedance | Cosine | Z | T.B.D. Ohm ± 20% | phi = 0° | 139.52 | T.B.D. Ohm | phi = 0° | 455.56 |
| | | L | ----- | | 2.21 | ----- | | 7.221 |
| | Sine | Z | T.B.D. Ohm ± 20% | | 137 | T.B.D. Ohm | | 464.67 |
| | | L | ----- | | 2.17 | ----- | | 7.374 |
| DC Resistance | Primary | | ----- | | 9.54 | T.B.D. Ohm | | 15.87 |
| | Cosine | | | | 13.46 | | | 43.75 |
| | Sine | | | | 14.89 | ----- | | 38.04 |
| Phase shift | | | T.B.D. ° ± 5° | | 3.045 | T.B.D. ° ± 5° | | 17.93 |
| Max. operating Speed | | | 22,000 rpm | | | 17,550 rpm | | |
| Operating temp. Range | | | -40°C - +150°C | | | -40°C - +150°C | | |
| | | | **Sensor Sample #4** | | | **Sensor Sample #5** | | |
| | | | Datasheet | | Validation | Datasheet | | Validation |
| Poles | | | 3 | | | 4 | | |
| Input Voltage | | | AC 7 Vrms 10 kHz | | | AC 7 Vrms 10 kHz | | |
| Transformation Ratio | | | 0.286 +/0.0286 | | 0.286 | 0.2 ± 0.02 | | 0.195 |
| Input Impedance | Z | | 100 ± 10 Ohm | | 101.36 | 50 ± 10 Ohm | | 45.36 |
| | L | | ----- | | 1.601 | ----- | | 0.713 |
| Output Impedance | Cosine | Z | T.B.D. Ohm | | 386.59 | T.B.D. Ohm | | 74.42 |
| | | L | ----- | | 6.14 | ----- | | 1.174 |
| | Sine | Z | T.B.D. Ohm | | 388.76 | T.B.D. Ohm | | 75.62 |
| | | L | ----- | | 6.177 | ----- | | 1.196 |
| DC Resistance | Primary | | T.B.D. Ohm ± 10% | | 12.61 | | | 7.07 |
| | Cosine | | | | 25.93 | ----- | | 8.75 |
| | Sine | | ----- | | 28.11 | | | 10.17 |
| Phase shift | | | T.B.D. ° | | 12.6 | T.B.D ° | | 16.2 |
| Max. operating Speed | | | 17,550 rpm | | | 24,000 rpm | | |
| Operating temp. Range | | | -40°C - +150°C | | | -40°C - +150°C | | |

Fig. 26. Benchmark overview for investigated sensor samples

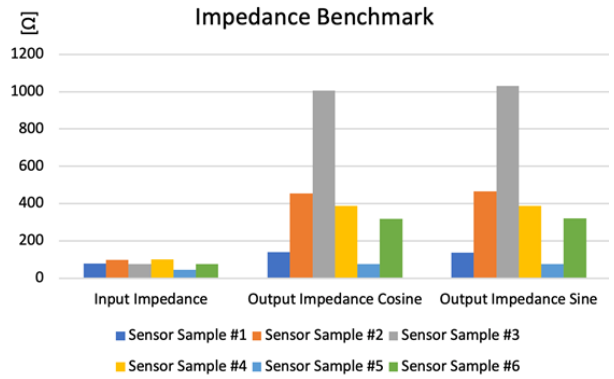


Fig. 27. Resolver impedance benchmark for Samples #1 to #6

**ISSN:** 2414-4592
**DOI:** 10.20474/jater-5.1.4

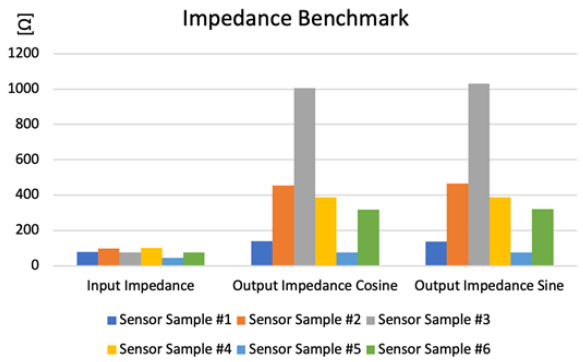


Fig. 28. Resolver DC resistance benchmark for Samples #1 to #6

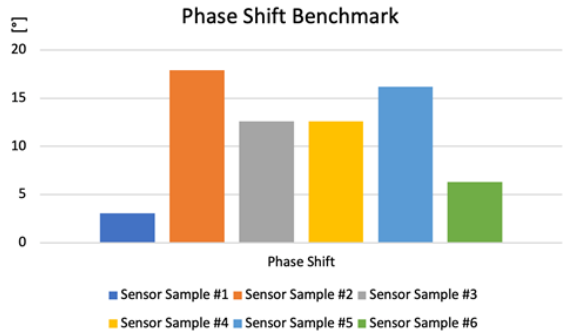


Fig. 29. Resolver electrical phase shift benchmark for Samples #1 to #6

At first sight the input impedance benchmark (Figure 26) shows that a typical resolver has a low input impedance but a high output impedance. This characteristic is necessary for the resolver's driver stage in the R2D of the vehicle's power train system and for the read in procedure of the analog feedback signals in the AFE of the R2D. Considering the output impedance, it is interesting to see that a resolver with a high number of pole pairs p (e.g., *Sample* #3, $p = 10$) has a higher output impedance than a resolver with less pole pairs (e.g., *Sample* #5, $p = 4$). Obviously, the impedance depends on the mechanic size (diameter) of the resolver, hence *Sample* #5 has a third of the diameter of *Sample* #3. Further, it can be seen in Figure 26, that the sine output coil has slightly a greater impedance than the cosine output coil. As stated in sub-section Resolver position sensor (Figure 2), the output coils are mechanically shifted by an offset of 90°. Hence there is mechanically only one location for the electric terminal, the assumption of this result is that the copper wires need to be a bit longer for one coil (here the sine output coil). This also shows, that the introduced measurement method is very accurate to point out design aspects of the resolver as well. Of course, the same statement applies to the DC resistance benchmark, Figure 27. Regarding the phase shift benchmark in Figure 28, it cannot be assumed that resolvers having less pole pairs have a lower phase shift, compared to resolvers with a high number of pole pairs. The phase shift characteristic in operation is very sensor layout specific.

In the design process of electric drive trains, the development of optimal machine control requires a comprehensive understanding of the position/speed sensor behavior. In this context, the benchmark results can support this process by provision of different resolver sensor characteristics. The driver stage of the R2D interface, which is included in the ECU, needs to supply the resolver. Hence the resolver has relatively high power consumption (see Figure 26 – Input Voltage), a resolver having a small input impedance is preferable (e.g., Sensor *Sample*#5, Figure 26). Less input impedance means less losses and so less driving current to excite the sensor. Another criterion of an optimal resolver driving stage is the excitation frequency stability. Since the DC resistance of the primary resolver side acts as a damping element, a lower DC resistance can cause resonance. This has to be considered when designing the controller's interface. As a result, the chosen sensor should hold a medium to high DC input resistance. When it comes to the angle determination of the electric machine's rotating shaft, the analog resolver feedback signals are fed into the Analog Front End (AFE) of the R2D. This AFE contains analog filters and OPAMPs. Typically, the AFE has a high-Ohmic input in the range of several kilo Ohms (kΩ) [28]. High input impedances at OPAMPs are widely used to achieve noise immunity. As in conventional electrical measurement, the sensor signal level needs to be high enough for a high-Ohmic amplifier input. When designing the AFE, the resolver's output impedance and DC resistance are important factors to achieve the optimal level of the source signals (resolver feedback signals) for the ECU inputs, in particular the AFE of the R2D. In operation mode of the electric drive train, the phase shift of the resolver is a very important parameter. A higher phase shift implies a larger time delay between the input- and output signal and so a wrong, delayed rotor shaft position. To reduce this latency, a resolver should be chosen that offers very little phase shift. If this is not possible, the sensor can be gauged regarding phase shift during the design process. The determined phase shift occurring under a certain speed could be stored e.g., in a look-up table on the powertrain's controller for online compensation while operation. An angular error can be caused by both, mechanical and electrical tolerances. Previous research investigated the influence of mechanical tolerances, where mechanical displacement can lead to distorted feedback signals, see [14]. Electrical sensor tolerances can cause effects

**ISSN:** 2414-4592
**DOI:** 10.20474/jater-5.1.4

regarding signal quality. Assuming impedance and resistance tolerances, damping in the excitation amplitude can occur, which leads to weak resolver feedback signals (see also Figure 6) that cause a faulty rotor position determination. For that reason, resolver rotor position sensors with minor tolerances should be preferred, which can be evaluated by the presented methods in this work. As stated in the subsection Temperature behavior analysis, the temperature has only a minor effect on the electric signal quality. Nevertheless, a temperature variation can cause a change in the coil resistance (Figure 24), which also leads to reduced feedback signal levels. It is well known that the resolver is a very robust sensor regarding magnetic fields and temperature influences, which is proven by the performed evaluations in this work.

## IV. CONCLUSION AND OUTLOOK

This paper extends the state-of-the-art rotor position sensor characterization for resolver technology by the investigation of electric sensor parameters. The introduced methods can be applied to determine missing parameters and for validating provided specifications. Different electrical analyses have been performed in this work such as DC analysis, AC analysis, impedance determination, transfer function determination. In addition, parasitic effects have been investigated. Therefore, it turned out, that these effects do not have a huge impact on the sensor's transfer function, especially in the mentioned area of operation. Apart from the mentioned analyses, the amplitude response is investigated in both, ideal mechanical position and displacement. The results show, that the alignment of the rotor affects the resolver's transfer ratio. The resolver sensor's transfer function itself shows no big difference compared to an ideal alignment. Also, an electrical phase analysis is performed in this work to identify the phase lag of the investigated resolver, since this is an important parameter when compensating time delays in the sensor system.

Three approaches are presented: XOR-gate, signal multiplication and estimation, whereby a combination of the second and the third method including the developed look-up table achieves the best representation of the phase lag. Tests have shown that the designed phase measurement circuit (multiplier) provides a very sensitive output voltage that enables a precise phase lag determination. A further analysis deals with the temperature investigation. Here, the results prove that the investigated sensor is very robust against temperature deviations. Hence small, linear changes in the resolver's resistance are determined, the idea of measuring the rotor temperature using the resolver came up. Using an additional Analog-to-Digital Converter (ADC) in the ECU, this resistance change in form of the electrical current can be determined. By the use of a look-up-table comprising current values for certain temperatures or the application of numerical regression, the rotor shaft temperature can be measured indirectly. This brings the advantage of redundant temperature measuring or reducing the number of sensors in the drive train system. A comprehensive benchmark comparing six different resolver types provides a detailed overview of each sensor's characteristic. This information might deliver data for designing a drive train and therefore choosing an appropriate resolver. Exemplary, it might be advantageous to choose Sensor Sample # 1 from the benchmark's result, since the signal latency (phase shift) is low compared to other samples in this test. Regarding the impedance, only Sensor Sample # 4 provides a lower impedance for input and output. This statement is also applicable for the DC resistance. Further, it is proven that the applied methods are correct, since their results match with the manufacturer- provided specifications. Thus, the introduced approach in this work enables to determine the not manufacturer- defined parameters and so supports the drive train system design. Future work will address the usage of the method and benchmark results for the R2D design process. Besides a novel concept considering indirect temperature determination using only a resolver and the ECU, is one prospective research topic. Additionally, concepts and algorithms will be developed to perform the introduced test methods automatically, which has a potential to reduce the test and evaluation effort to a minimum and thus enables cost saving in pre-development processes.

## REFERENCES

[1] L. Szabo, ``Integrated starter-generators for automotive applications,'' *Journal of Technical University of Cluj-Napoca*, vol. 45, no. 3, pp. 256-260, 2004.

[2] H. U. Rehman, ``An integrated starter-alternator and low-cost high-performance drive for vehicular applications,'' *IEEE Transactions on Vehicular Technology*, vol. 57, no. 3, pp. 1454-1465, 2008. doi: https://doi.org/10.1109/tvt.2007.909255

[3] J. Joonwoo, H. K. Dong, C. Bumsuk, K. Geonwoo, and S. K. Yoo, ``A construction of vehicle image and ground truth database for developing vehicle maker and model recognitions,'' *International Journal of Technology and Engineering*

*Studies*, vol. 3, no. 6, pp. 229-235, 2017. doi: https://doi.org/10.20469/ijtes.3.40002-6

[4] S. N. Cubero, S. McLernon, and A. Sharpe, ``Over-speeding warning system using wireless communications for road signs and vehicles,'' *Journal of Advances in Technology and Engineering Studies*, vol. 2, no. 5, pp. 140-155, 2016. doi: https://doi.org/10.20474/jater-2.5.2

[5] J. Dixon and C. Garcés, ``Binary position sensor for synchronous machines based on a serial n-bit sequential code,'' in *Eighth International Conference and Exhibition on Ecological Vehicles and Renewable Energies (EVER),* California, CA, 2013.

[6] H. A. S. Fadrah, A. Z. Kamarul, A. Mohd, Basri, and A. Y. Mohd, ``Fatigue damage simulation of automobile steering knuckle subjected to variable amplitude loading,'' *International Journal of Technology and Engineering Studies*, vol. 3, no. 6, pp. 245-252, 2017. doi: https://doi.org/10.20469/ijtes.3.40004-6

[7] F. Tootoonchian, ``Proposal of a new affordable 2-pole resolver and comparing its performance with conventional wound-rotor and VR resolvers,'' *IEEE Sensors Journal*, vol. 18, no. 13, pp. 5284-5290, 2018. doi: https://doi.org/10.1109/jsen.2018.2834552

[8] Minebea Mitsumi, ``Rotation angle sensor (resolver) for ev/hev drive motor,'' n.d. [Online]. Available: https://bit.ly/376wQXR

[9] W. Wanja, L. Daniela, and R. Linda, ``Sustainability in automotive interior–comparison of volume and premium brand manufacturers,'' *Journal of Advances in Technology and Engineering Studies*, vol. 4, no. 5, pp. 197-206, 2018. doi: https://doi.org/10.20474/jater-4.5.3

[10] C. Wang and X. Qian, ``A new kind of resolver-to-digital method for motor drive,'' in *IEEE Conference and Expo Transportation Electrification Asia-Pacific (ITEC Asia-Pacific),* Tokyo, Japan, 2014.

[11] C. Datlinger and M. Hirz, ``Investigations of rotor shaft position sensor signal processing in electric drive train systems,'' in *IEEE Transportation Electrification Conference and Expo, Asia-Pacific (ITEC Asia-Pacific),* Istanbul, Turkey, 2018.

[12] C. Datlinger, and M. Hirz, ``Evaluation of signal processing effects on rotor position sensor systems for electric traction motors,'' in *Conference EAEC,* Hague, Neitherland, 2017.

[13] C. Datlinger and M. Hirz, ``An extended approach for validation and optimization of position sensor signal processing in electric drive trains,'' *Electronics*, vol. 8, no. 1, pp. 77-80, 2019. doi: https://doi.org/10.3390/electronics8010077

[14] J. Gaechter, ``Evaluation of rotor position sensor characteristics and impact on control quality of permanent magnet synchronous machines,'' Ph.D. thesis, Graz University of Technology, Graz, Austria, 2017.

[15] X. Yongxiang, Z. Dianchen, W. Yanyu, Z. Jibin, and S. Jing, ``Dsp based all-digital resolver-to-digital conversion using DSRF-PLL,'' in *Proceedings of The 7th International Power Electronics and Motion Control Conference,* Beijing, China, 2012.

[16] N. Neidig, Q. Werner, M. Balluff, H. Naumoski, and M. Doppelbauer, ``The influence of geometrical deviations of electrical machine systems on the signal quality of the variable reluctance resolver,'' in *6th International Electric Drives Production Conference (EDPC),* New Dehli, India. IEEE, 2016.

[17] C.-C. Hou and H.-W. Lin, ``Dsp-based 3d printed resolver-to-digital conversion system,'' in *IEEE 11th International Conference on Power Electronics and Drive Systems,* Sydney, Austraila, 2015.

[18] S. Tamagawa, ``Encoders UK-the leading tamagawa encoder supplier,'' 2019. [Online]. Available: https://bit.ly/2QkLpB3

[19] J. O. Attia, ``Two-port networks-electronics and circuit analysis using matlab,'' 1999. [Online]. Available: https://bit.ly/2QvOwGD

[20] R. Wang, ``Two port networks,'' 2019. [Online]. Available: https://bit.ly/2CHfgf4

[21] PSpice, ``Electronic circuit optimization & simulation | cadence pspice,'' 2019. [Online]. Available: https://bit.ly/2NOJC5B

[22] Graz University of Technology, ``FTG-institute of automotive engineering Graz,'' n.d. [Online]. Available: https://bit.ly/2XkBVqT

[23] C. Stehning, A. Buhrdorf, and J. Binder, ``Mebtechniken und schaltungsentwurfe zur hochprazisen abstandsmessung mit ultraschal,'' 2019. [Online]. Available: https://bit.ly/2QgR630

[24] F. E. Coffield, ``A high-performance digital phase comparator,'' *IEEE Transactions on Instrumentation and Masurement*, no. 3, pp. 717-720, 1987. doi: https://doi.org/10.1109/tim.1987.6312777

**ISSN:** 2414-4592
**DOI:** 10.20474/jater-5.1.4

[25] Texas Instruments, ``LM319-N: dual high speed, high voltage comparator,'' 2018. [Online]. Available: https://bit.ly/2KopKV0
[26] Texas Instruments, ``Cd74hct86 xor: High-speed CMOS logic quad 2-input exclusive-or gate,'' 2018. [Online]. Available: https://bit.ly/33Qag3J
[27] Analog Devices, ``Low cost analog multiplier AD633,'' 2018. [Online]. Available: https://bit.ly/2Km5oLQ
[28] Texas Instruments, ``PGA411-Q1 resolver sensor interface: Datasheet texas instruments,'' 2019. [Online]. Available: https://bit.ly/377PcaP

**ISSN:** 2414-4592
**DOI:** 10.20474/jater-5.1.4